

SnO_2/Co_3O_4 nanofibers using double jets electrospinning as low operating temperature gas sensor

Zhao Wang(王昭), Shu-Xing Fan(范树兴), and Wei Tang(唐伟)

Citation: Chin. Phys. B, 2022, 31 (**2**): 028101. DOI: 10.1088/1674-1056/ac1336
Journal homepage: http://cpb.iphy.ac.cn; http://iopscience.iop.org/cpb

What follows is a list of articles you may be interested in

Thermal conductivity characterization of ultra-thin silicon film using the ultra-fast transient hot strip method

Yan-Yan Zhang(张燕燕), Ran Cheng(程然), Dong Ni(倪东), Ming Tian(田明), Ji-Wu Lu(卢继武), Yi Zhao(赵毅)
Chin. Phys. B, 2019, 28 (**7**): 078105. DOI: 10.1088/1674-1056/28/7/078105

Synthesis and characterization of β-Ga_2O_3@GaN nanowires

Shuang Wang(王爽), Yue-Wen Li(李悦文), Xiang-Qian Xiu(修向前), Li-Ying Zhang(张丽颖), Xue-Mei Hua(华雪梅), Zi-Li Xie(谢自力), Tao Tao(陶涛), Bin Liu(刘斌), Peng Chen(陈鹏), Rong Zhang(张荣), You-Dou Zheng(郑有炓)
Chin. Phys. B, 2019, 28 (**2**): 028104. DOI: 10.1088/1674-1056/28/2/028104

Large scale fabrication of nitrogen vacancy-embedded diamond nanostructures for single-photon source applications

Qianqing Jiang(姜倩晴), Wuxia Li(李无瑕), Chengchun Tang(唐成春), Yanchun Chang(常彦春), Tingting Hao(郝婷婷), Xinyu Pan(潘新宇), Haitao Ye(叶海涛), Junjie Li(李俊杰), Changzhi Gu(顾长志)
Chin. Phys. B, 2016, 25 (**11**): 118105. DOI: 10.1088/1674-1056/25/11/118105

Large-scale photonic crystals with inserted defects and their optical properties

Li Chao-Rong, Li Juan, Yang Hu, Zhao Yong-Qiang, Wu Yan, Dong Wen-Jun, Chen Ben-Yong
Chin. Phys. B, 2014, 23 (**8**): 088114. DOI: 10.1088/1674-1056/23/8/088114

Templated synthesis of highly ordered mesoporous cobalt ferrite and its microwave absorption properties

Li Guo-Min, Wang Lian-Cheng, Xu Yao
Chin. Phys. B, 2014, 23 (**8**): 088105. DOI: 10.1088/1674-1056/23/8/088105

SnO_2/Co_3O_4 nanofibers using double jets electrospinning as low operating temperature gas sensor

Zhao Wang(王昭), Shu-Xing Fan(范树兴), and Wei Tang(唐伟)†

School of Physics and Electronics, Shandong Normal University, Jinan 250358, *China*

(Received 25 April 2021; revised manuscript received 28 June 2021; accepted manuscript online 12 July 2021)

SnO_2/Co_3O_4 nanofibers (NFs) are synthesized by using a homopolar electrospinning system with double jets of positive polarity electric fields. The morphology and structure of SnO_2/Co_3O_4 hetero-nanofibers are characterized by using field emission scanning electron microscope (FE-SEM), transmission electron microscope (TEM), x-ray diffraction (XRD), and x-ray photoelectron spectrometer (XPS). The analyses of SnO_2/Co_3O_4 NFs by EDS and HRTEM show that the cobalt and tin exist on one nanofiber, which is related to the homopolar electrospinning and the crystallization during sintering. As a typical n-type semiconductor, SnO_2 has the disadvantages of high optimal operating temperature and poor reproducibility. Comparing with SnO_2, the optimal operating temperature of SnO_2/Co_3O_4 NFs is reduced from 350 °C to 250 °C, which may be related to the catalysis of Co_3O_4. The response of SnO_2/Co_3O_4 to 100-ppm ethanol at 250 °C is 50.9, 9 times higher than that of pure SnO_2, which may be attributed to the p–n heterojunction between the n-type SnO_2 crystalline grain and the p-type Co_3O_4 crystalline grain. The nanoscale p–n heterojunction promotes the electron migration and forms an interface barrier. The synergy effects between SnO_2 and Co_3O_4, the crystalline grain p–n heterojunction, the existence of nanofibers and the large specific surface area all jointly contribute to the improved gas sensing performance.

Keywords: SnO_2/Co_3O_4 nanofibers (NFs), homopolar double jets electrospinning, gas sensors, nanoscale p–n heterojunction

PACS: 81.16.–c, 81.07.–b, 85.35.–p **DOI:** 10.1088/1674-1056/ac1336

1. Introduction

Volatile organic compounds (VOCs) are important precursors for the formation of secondary pollutants such as fine particulate matter 2.5 (PM2.5) and ozone (O_3), which lead to atmospheric environmental problems such as haze and photochemical smog. It does great harm to the natural environment and human health. Therefore, it is necessary to develop a generalized gas sensor for VOCs, in order to carry out comprehensive prevention and control of VOCs pollution.

Chemical resistance gas sensor based on metal oxide semiconductors (MOSs)[1,2] has been widely studied in the detection of toxic and explosive gases because of its simple operation, low cost and high sensitivity. So far, a large number of MOSs have been studied, such as SnO_2,[3–6] ZnO,[7–10] In_2O_3,[11] and CuO.[12] Tin oxide (SnO_2) based on the change of resistance to detect VOCs has attracted special attention due to its high sensitivity and good stability.[13,14] However, the pure SnO_2 gas sensor has some disadvantages, such as poor selectivity, high operating temperature, long recovery time, *etc*.[15,16] Therefore, the doping and compounding of SnO_2 gas sensor, such as noble metal elements or other metal oxide semiconductors, organic compounds, *etc*., make SnO_2-based gas sensor show better gas sensing characteristics than pure SnO_2 gas sensor.[17–21]

After mixing the n-type SnO_2 with other metal–oxide semiconductors, the formation of heterojunction can adjust the barrier height, expand the electron depletion layer, and produce a synergistic effect on the interface, to improve the gas sensing characteristics of SnO_2-based gas sensors.[22–26] By compounding with different metal–oxide semiconductors, gas sensing materials with different gas sensing characteristics may be obtained. The Co_3O_4 is a p-type semiconductor. Owing to the large energy gap between Co_3O_4 band gap (1.63 eV)[27] and SnO_2 band gap (3.8 eV),[28,29] the p–n heterojunction is formed after SnO_2 and Co_3O_4 have been combined, which leads the carriers to migrate between SnO_2 and Co_3O_4, thus forming the depletion layer and the high barrier layer.[30,31] This makes the target gas produce more hot spots when it contacts the gas sensing material. The p–n heterojunction is formed by the combination of MOSs with different conductive types. The p–n heterojunction can regulate the band gap of semiconductor, thereby forming the impurity energy levels, which can change the electrical properties of the material surface.

The formation of nanoscale p–n heterojunction promotes the additional oxygen to adsorb on the surface, and Co_3O_4 also has a catalytic activity, which may improve the gas sensing characteristics at low temperatures. Therefore, Co_3O_4/SnO_2 composite can be used as a good gas sensing nanocomposite. It is reported that the SnO_2/Co_3O_4 nanoscale heterojunction has been formed, and the detection of acetone has been greatly improved.[32,33] Co-doped SnO_2 nanofibers showed the highest response toward 100-ppm ethanol.[1] The

†Corresponding author. E-mail: tangweiyouxiang@foxmail.com

© 2022 Chinese Physical Society and IOP Publishing Ltd

$0.5SnO_2/0.5Co_3O_4$ sensor has a good response to C_6H_6 at 350 °C.[30]

The one-dimensional nanofiber material prepared by the electrospinning technology can significantly improve the response of the VOCs gas sensor due to its large specific surface area and high porosity. The homopolar doublejet electrospinning technology can mix the precursor solutions of two different metal oxide semiconductors, which is different from the traditional solution mixed electrospinning[34–36] and double jets of positive and negative polarity electric fields.[37]

The homopolar doublejet electrospinning technology can effectively ensure that the nanoscale heterojunction forms between the two kinds of precursor solutions, and prevent the different precursor solutions from clustering. The SnO_2 is compounded with Co_3O_4 in this work, and its gas sensing function is systematically investigated. Themorphologies, chemical compositions and element chemical states of the samples are characterized by XRD, SEM, TEM, EDS, and XPS. The SnO_2/Co_3O_4 nanofibers (NFs) have better gas sensing characteristics than the SnO_2 NFs, such as lower detection limit, lower operating temperature and better selectivity. The gas sensing properties and mechanism of SnO_2/Co_3O_4 NFs are also discussed.

2. Experiment

2.1. Fabrication of SnO_2/Co_3O_4 NFs-based gas sensors

Analytical grade chemicals without further purification were used in the experiment. The SnO_2/Co_3O_4 NFs were prepared by two stages including electrospinning and annealing. The electrospinning precursors of SnO_2 and Co_3O_4 were incorporated into two identical 10-ml syringes, respectively. The syringe contains 6 ml of ethanol, 7 ml of 2N-dimethylformamide (DMF), 900 mg of polyvinyl pyrrolidone (PVP, $M_w = 1.3 \times 10^6$), 900 mg of $Co(NO_3)_2{\cdot}6H_2O$ or 700 mg of $SnCl_2{\cdot}2H_2O$ after having been stirred magnetically for 10 h. The molar ratio of $Co(NO_3)_2{\cdot}6H_2O$ to $SnCl_2{\cdot}2H_2O$ was 1:1. The PVP/$SnCl_2{\cdot}2H_2O$ and PVP/$Co(NO_3)_2{\cdot}6H_2O$ composite precursors were prepared by homopolar double jets electrospinning. The ratio of Sn to Co could be controlled by setting different propulsion speeds. The schematic diagram of the homopolar doublejet electrospinning device is shown in Fig. 1. In the electrospinning process, the distance between the syringe tip and the aluminum plate collector was fixed at 25 cm, and the potential between the needle tip and the aluminum plate was maintained at 20 kV. The platform moved back and forth with a speed of 20 cm/min. The calcining precursor was collected on the aluminum plate collector and calcined in the crucible. In the calcination process in the muffle furnace, it was annealed at 300 °C for 2 h with a heating rate of 2 °C/min to ensure the volatilization of PVP, and at 500 °C for 2 h to be crystallized, and SnO_2/Co_3O_4 NFs were collected after natural cooling. Four kinds of SnO_2/Co_3O_4 NFs, *i.e.*, Sn : Co = 1 : 6, Sn : Co = 1 : 3, Sn : Co = 1 : 1, and Sn : Co = 3 : 1 were prepared at different propulsion speeds of syringe. The obtained samples were named SnO_2/Co_3O_4-1, SnO_2/Co_3O_4-2, SnO_2/Co_3O_4-3, and SnO_2/Co_3O_4-4, respectively. The pure SnO_2 and Co_3O_4 NFs were prepared by the same process with only one syringe.

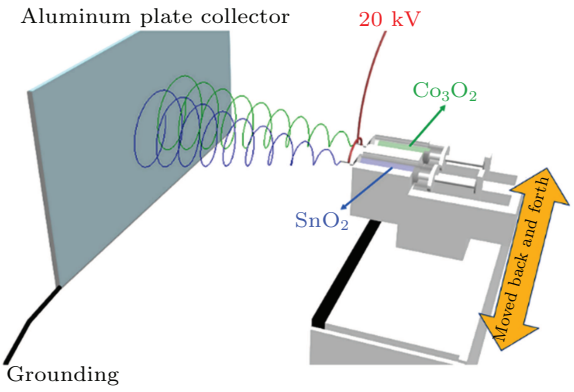


Fig. 1. Schematic illustration of homopolar doublejet electrospinning setup.

2.2. Characterization

The crystalline structures of samples were recorded by Bruker D8 Advance x-ray powder diffraction (XRD), diffractometer with Cu $K\alpha$ radiation and a wavelength of 1.54176 Å over the 2θ range from 10°–80° in steps of 0.03°. The sample morphology was studied using a Sigma500 field emission scanning microscopy (FE-SEM) and Fei Tecnai G2 F20 field emission transmission electron microscope (FE-TEM). The elemental distribution of the sample was characterized by x-ray energy dispersive spectrometer (EDS) equipped with SEM. The x-ray photoelectron spectrometer (XPS) data were obtained by using Thermpfisher EscaLab 250Xi.

2.3. Measurement of gas sensing properties

The calcined sample was mixed with deionized water in an agate mortar and grinded it into a paste in a certain direction. The paste was evenly coated on the ceramic tube and dried overnight at room temperature to obtain gas sensors. The gas sensitivity was tested by an intelligent gas sensing analysis system (CGS-8). Owing to the existence of nanoscale p–n heterojunction between SnO_2/Co_3O_4 NFs, the resistance of the composite increased and exceeded the upper limit of CGS-8 resistance measurement (500 MΩ). Therefore, the paste was coated on the planar platinum electrode and the gas sensitivity was tested by using the comprehensive gas sensing test platform CGS-MT. The VOCs (the inference gases for gas selectivity testing include methanol, formaldehyde, acetone, ammonia, and ethanol) selectivity, the optimum operating temperature and the response (1 ppm–100 ppm concentration) of

the prepared gas sensor were studied. All sensors were aged at 300 °C for 10 h/time for 3 times prior to measurement.

3. Results and discussion

3.1. Microstructures

Figures 2(a)–2(c) show the morphology of SnO_2 NFs, Co_3O_4 NFs, and SnO_2/Co_3O_4 NFs, respectively. Figure 2 shows that all NFs are relatively uniform with diameters in a range of 100 nm–150 nm. In Fig. 2(c), it is impossible to judge whether the nanofibers are SnO_2/Co_3O_4 NFs or single NFs, so the SnO_2/Co_3O_4 NFs are characterized by EDS, and the results are shown in Fig. 3. Tin, cobalt and oxygen appear on one nanofiber. It can be found from Figs. 3(c)–3(e) that the elements of Sn, Co and O are uniformly distributed, but the content of Co is clearly less than that of Sn.

The TEM images of SnO_2/Co_3O_4 NFs in Figs. 4(a) and 4(b) show that the sizes and morphologies are similar to the results of SEM. In order to further confirm the composites of SnO_2 and Co_3O_4 on the same nanofiber, the samples are characterized by HRTEM as shown in Fig. 4(c). The lattice fringes can be observed and the lattice spacings are 0.287 nm and 0.24 nm, corresponding to the (220) plane and (311) plane of Co_3O_4, respectively. It can be seen from Fig. 4(c) that the lattice fringes with 0.325 nm and 0.328 nm correspond to the crystal plane (110) of SnO_2. The lattice fingerprint of SnO_2/Co_3O_4 NFs is consistent with the XRD pattern (Fig. 6).

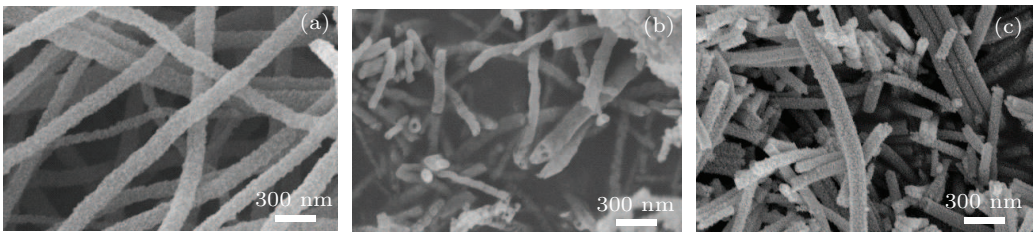


Fig. 2. SEM images of (a) SnO_2, (b) Co_3O_4, (c) SnO_2/Co_3O_4 NFs.

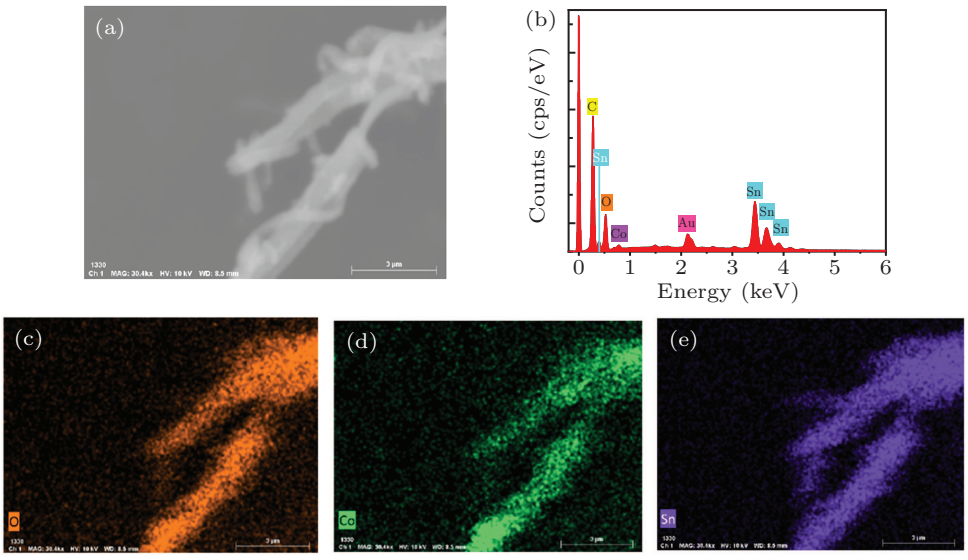


Fig. 3. EDS of (a) SnO_2/Co_3O_4 and (b) its mapping, EDS of (c) O element, (d) Sn element, and (e) Co element.

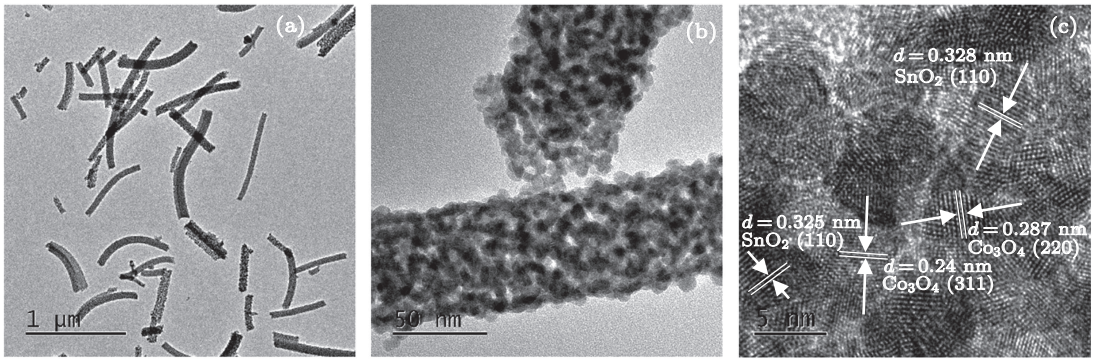


Fig. 4. (a) and (b) TEM images of SnO_2/Co_3O_4 NFs and (c) HRTEM of lattice fringes of SnO_2/Co_3O_4 NFs.

The SnO_2/Co_3O_4 NFs have been compounded in the process of double jets electrospinning, which can be proved by the fact that the initially spun nanofibers collected by aluminum plate are blue. Homopolar doublejet electrospinning makes the two materials contact alternately during collection. Under the influence of positive high voltage electrode, the reaction of $PVP/SnCl_2{\cdot}2H_2O$ and $PVP/Co(NO_3)_2{\cdot}6H_2O$ in doublejet electrospinning can occur as follows:

$$2[Co(6H_2O)]^{2+} + 4Cl^- = Co(CoCl_4) + 12H_2O, \quad (1)$$

where $[Co(6H_2O)]^{2+}$ is an octahedral complex, and $(CoCl_4)^{2-}$ is a tetrahedral complex. The spectral absorption intensity of the tetrahedral complex is higher than that of the octahedron, so the composite fiber shows light blue.

In the calcination process, the electrospinning precursors form a hollow nanofiber structure due to the Kirkendall effect.[38–40] As shown in Fig. 5, tin and cobalt ions on the surface of the nanofibers are oxidized, while the internal ones are not oxidized due to hypoxia. The PVP on the surface of the nanofibers is calcined and volatilized, and the PVP inside is in a molten state. The PVP concentration difference between the inside and outside of the nanofiber is formed, while the diffusion rate of the molten PVP is faster, carrying tin and cobalt ions to the surface of the nanofibers to be calcined, forming a hollow nanofiber structure and further compounding.

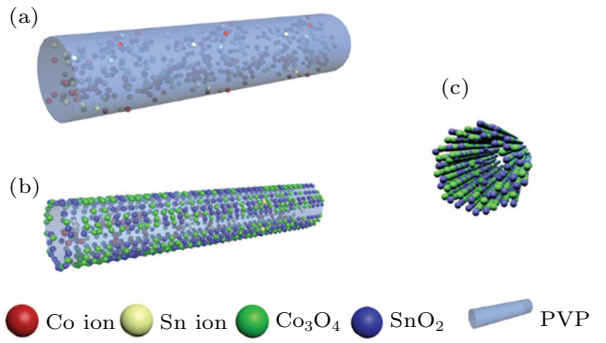


Fig. 5. Schematic diagram of calcination process model (a) prior to calcination, (b) calcining, (c) as-calcined.

As shown in Fig. 6, the crystal structures of SnO_2 NFs, Co_3O_4 NFs and SnO_2/Co_3O_4 NFs are characterized by XRD. The diffraction peaks of pure SnO_2 are observed to be at 2θ of 26.579, 33.864, 37.941, 38.965, 42.625, 51.756, 54.740, 57.804, 61.861, 64.714, and 65.943, which belong to (110), (101), (200), (111), (210), (211), (220), (002), (310), (112), and (301) crystal planes of tetragonal rutile SnO_2 (PDF No. 99-0024), respectively. The results show that the (111), (220), (311), (222), (400), (511), and (440) crystal faces of Co_3O_4 correspond to the 2θ values of 18.999, 31.270, 36.845, 38.547, 44.808, 59.354, and 65.233, respectively, and the absorption peaks match well with those in the standard figure of Co_3O_4 (PDF No. 74-2120). There are characteristic diffraction peaks of Co_3O_4 in the curves of SnO_2/Co_3O_4-1, SnO_2/Co_3O_4-2, SnO_2/Co_3O_4-3, and SnO_2/Co_3O_4-4, which indicates that Co_3O_4 has been successfully loaded on SnO_2. No diffraction peaks of other phases are detected, implying high purity of the sample.

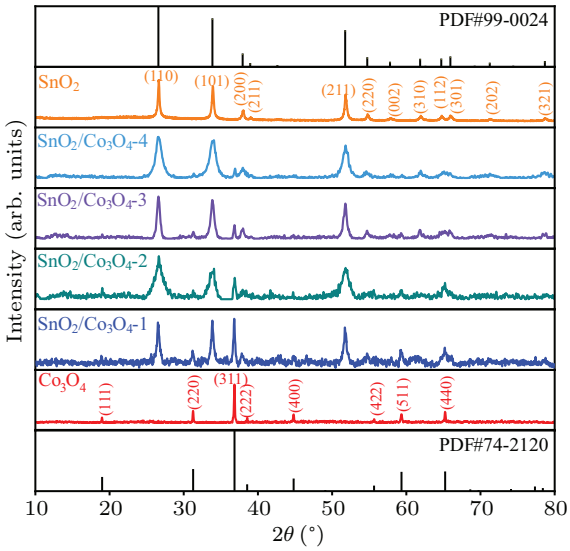


Fig. 6. XRD patterns of SnO_2NFs, SnO_2/Co_3O_4-4, SnO_2/Co_3O_4-3, SnO_2/Co_3O_4-2, SnO_2/Co_3O_4-1, and Co_3O_4 NFs.

The chemical compositions of the SnO_2 NFs, Co_3O_4 NFs, SnO_2/Co_3O_4-4 are characterized by XPS as shown in Fig. 7. All the spectra are corrected by the standard C 1s binding energy at 284.8 eV. The survey XPS spectra in Fig. 7(a) indicate the existence of Sn, Co, O, and C in SnO_2/Co_3O_4-4. It is found that the peak position of the binding energy for each of Sn and Co is shifted, which may be due to the formation of nanoscale p–n heterojunction, which produces new hot spots and makes more oxygen anion adsorb on the surface, resulting in the change of binding energy. The Sn 3d spectrum is shown in Fig. 7(b), and the SnO_2/Co_3O_4 NFs signal located at 495.0 eV and 486.5 eV are assigned to Sn $3d_{3/2}$ and Sn $3d_{5/2}$, respectively. The Co 2p and O 1s are separated into peaks as shown in Figs. 7(c) and 7(d). The Co 2p spectrum in Fig. 7(c) has two main peaks (796.9 eV and 780.8 eV) and two satellite peaks (802.3 eV and 786.4 eV). The two main peaks are assigned to Co $2p_{1/2}$ and Co $2p_{3/2}$, respectively. Both Co $2p_{1/2}$ and Co $2p_{3/2}$ can be divided into two peaks corresponding to Co^{2+} and Co^{3+}.[41,42] The crystal phase of Co_3O_4 is further confirmed. The O 1s spectrum in Fig. 7(d) can be divided into three peaks corresponding to three components: lattice oxygen (O_{latt} 530.22 eV), adsorbed oxygen (O_{ads} 530.52 eV), and surface oxygen (O_{surf} 531.72 eV).[42,43] The surface oxygen species of SnO_2 and SnO_2/Co_3O_4-4 are shown in Table 1. The amount of O_{ads} is very important for the sensing performance of sensor material. The O_{ads} of SnO_2/Co_3O_4-4 (37.4%) is much higher than that of pure SnO_2 (21.3%), which plays a positive role in improving the gas sensing performance. This may be due to the catalytic performance of Co_3O_4 promoting the oxygen adsorption of SnO_2. In Table 1, the atomic percentages of SnO_2 and SnO_2/Co_3O_4-4 are analyzed by XPS, which shows that the ratio of Sn to Co is very close to the theoretical ratio.

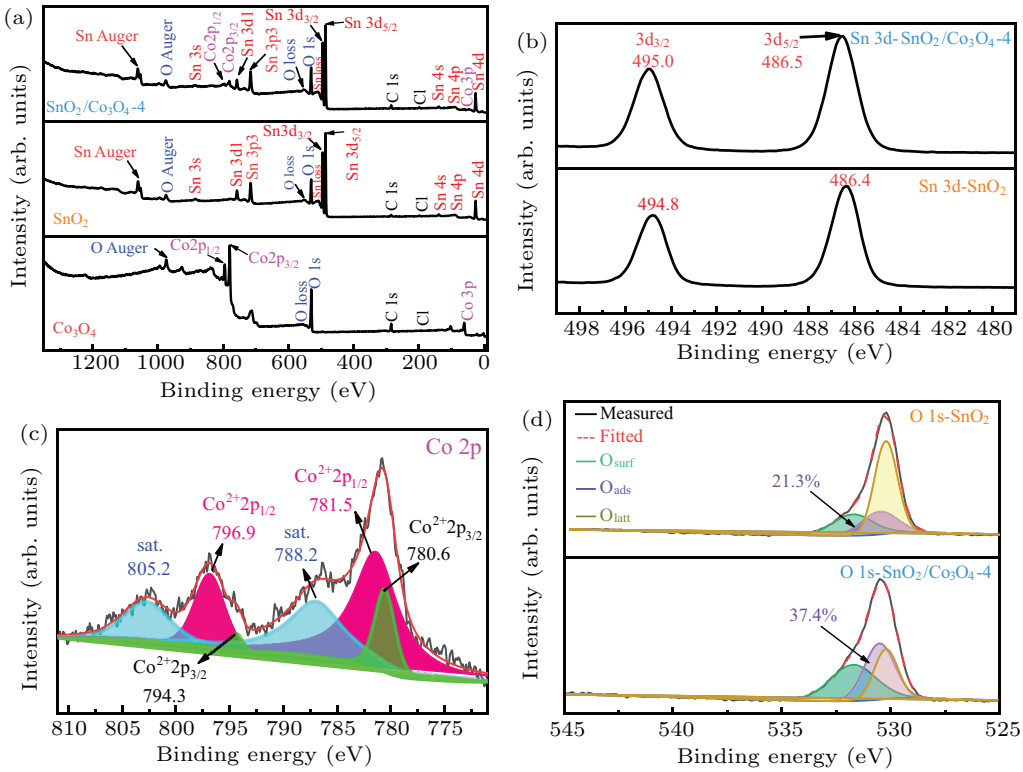


Fig. 7. XPS about (a) survey spectrums of SnO_2/Co_3O_4-4, SnO_2, and Co_3O_4; (b) Sn 3d of SnO_2/Co_3O_4-4 and SnO_2; (c) Co 2p of SnO_2/Co_3O_4-4, (d) O 1s of SnO_2 and Co_3O_4-4.

Table 1. Relative percentages of three oxygen components, atomic percentages of SnO_2 and SnO_2/Co_3O_4-4.

Samples	Surface oxygen species			Atomic %			
	O_{latt} (%)	O_{surf} (%)	O_{ads} (%)	C 1s	O 1s	Sn 3d	Co 2p
SnO_2	22.51	56.46	21.3	12.97	62.19	24.84	
SnO_2/Co_3O_4-4	26.29	36.40	37.4	20.15	54.69	18.78	6.38

3.2. Sensing properties

The response (R) of the SnO_2 and SnO_2/Co_3O_4-2, SnO_2/Co_3O_4-3, SnO_2/Co_3O_4-4 are defined as $R = R_a/R_g$. The response (R) of Co_3O_4 and SnO_2/Co_3O_4-1 are defined as $R = R_g/R_a$, where R_a is the stable resistance in air, and R_g is the stable resistance in probe gas.

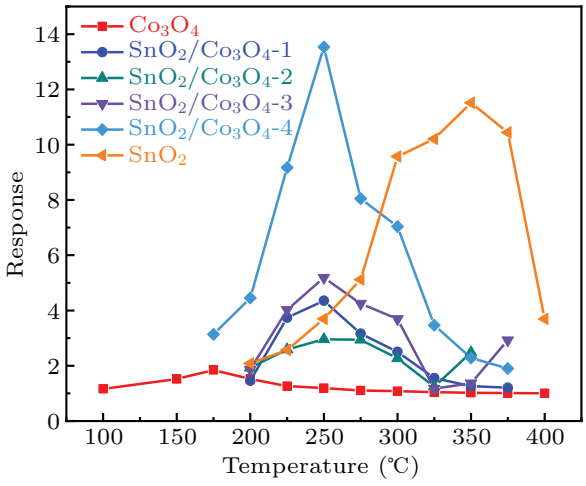


Fig. 8. Curves of response of SnO_2, Co_3O_4, and SnO_2/Co_3O_4 NFs sensors to 100-ppm ethanol *versus* operating temperature.

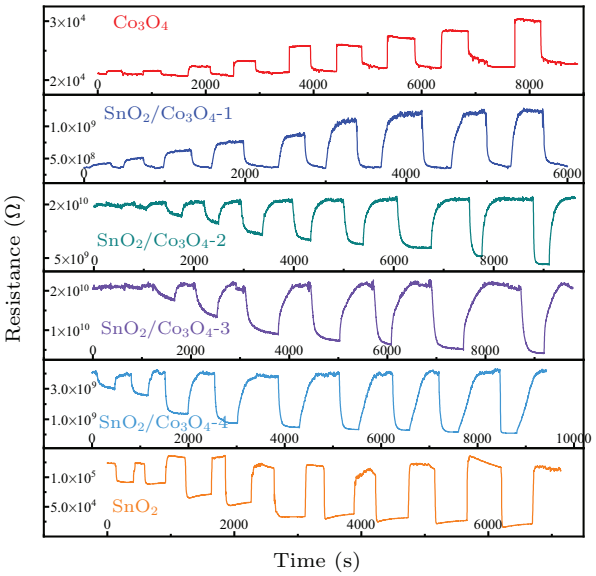


Fig. 9. Transient ethanolsensing properties of gas sensors based on Co_3O_4, SnO_2/Co_3O_4-1, SnO_2/Co_3O_4-2, SnO_2/Co_3O_4-3, SnO_2/Co_3O_4-4, and SnO_2 at operating temperature 250 °C.

The operating temperature strongly influences the response property of a semiconductor gas sensor. Figure 8 shows the gas sensing response of SnO_2, Co_3O_4, and SnO_2/Co_3O_4

NFs to 100-ppm ethanol versus operating temperature. Optimum operating temperature of SnO_2 sensor to 100-ppm ethanol is 350 °C, which is a typical disadvantage of SnO_2 sensor. Compared with the optimum operating temperature of the SnO_2 sensor, Co_3O_4 sensor's is lower, only 175 °C. The SnO_2/Co_3O_4 NFs shows the maximum response at 250 °C, and the SnO_2/Co_3O_4-4 has the highest response at 250 °C. The SnO_2/Co_3O_4-4 reduces the optimum operating temperature based on SnO_2 gas sensor.

Figure 9 shows the dynamic curves of response and recovery transient properties of Co_3O_4, SnO_2/Co_3O_4-1, SnO_2/Co_3O_4-2, SnO_2/Co_3O_4-3, SnO_2/Co_3O_4-4, and SnO_2 NFs gas sensors, respectively. The gas sensing properties are tested with ethanol at 250 °C. In Fig. 9 from the left to the right are the responses at 1 ppm, 2 ppm, 5 ppm, 10 ppm, 20 ppm, 30 ppm, 40 ppm, 50 ppm, 100 ppm, respectively. The conduction types of Co_3O_4 and SnO_2/Co_3O_4-1 are p-type, and the conduction types of SnO_2/Co_3O_4-2, SnO_2/Co_3O_4-3, SnO_2/Co_3O_4-4, and SnO_2 are n-type. The type of conduction depends on the content of n-SnO_2 and p-Co_3O_4 in the sample. When the ratio of SnO_2 to Co_3O_4 is 1:1 (the ratio of Sn to Co is 1:3 for SnO_2/Co_3O_4-2), the sensing behavior of the composite is of n-type, it is due to the contribution of electrons being greater than that of holes.[32] The SnO_2/Co_3O_4 NFs sensor can return to the initial resistance when exposed to air after different concentrations of ethanol have been injected, which indicates that the Co_3O_4/SnO_2 NFs sensor has good reproducibility. The resistance of SnO_2 NFs changes differently after the response has been recovered. Serving as a kind of gas sensor, the SnO_2 NFs have the disadvantage of poor reproducibility. When the ethanol concentration is 100 ppm, the response of SnO_2/Co_3O_4-4, SnO_2, and Co_3O_4 are of 50.60, 5.79, and 1.36, respectively. The synergistic effect of SnO_2 and Co_3O_4 makes SnO_2/Co_3O_4-4 have higher response and better reproducibility. It can be seen from the Fig. 9 that the resistance of composite material is much greater than that of single material, which may be due to the narrowing of electron transmission channel caused by the formation of nanoscale p–n heterojunction.

Figure 10 shows the selectivity of Co_3O_4, SnO_2/Co_3O_4-1, SnO_2/Co_3O_4-2, SnO_2/Co_3O_4-3, SnO_2/Co_3O_4-4, and SnO_2 to 40-ppm inference gases at 250 °C; the inference gases for gas selectivity testing include ethanol, methanol, formaldehyde, acetone, and ammonia. The sensor of SnO_2/Co_3O_4-4 shows the highest response to ethanol. The ethanol response of SnO_2/Co_3O_4-4 is 10.80, which is higher than that of SnO_2 (3.23), and Co_3O_4 (1.14), respectively. The sensing characteristics are summarized in Table 2.

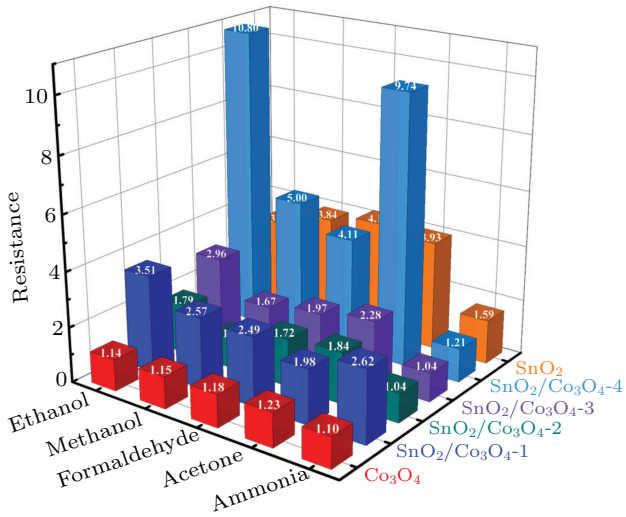


Fig. 10. Response of gas sensors based on the Co_3O_4, SnO_2/Co_3O_4-1, SnO_2/Co_3O_4-2, SnO_2/Co_3O_4-3, SnO_2/Co_3O_4-4, and SnO_2 to 40-ppm formaldehyde, methanol, ethanol, ammonia, and acetone at operating temperature 250 °C.

Table 2. Summary of sensing characteristics.

Samples	Sensing behavior	Optimum operating temperature (°C)	Response (250 °C, 100 ppm)	Selectivity	
				Gas	Response
Co_3O_4	p-type	175	1.36	acetone	1.36
SnO_2/Co_3O_4-1	p-type	250	3.07	ethanol	3.51
SnO_2/Co_3O_4-2	n-type	250	4.38	acetone	1.84
SnO_2/Co_3O_4-3	n-type	250	5.30	ethanol	2.96
SnO_2/Co_3O_4-4	n-type	250	50.60	ethanol	10.8
SnO_2	n-type	350	5.79	formaldehyde	4.11

3.3. Gas sensing mechanism

The gas sensing characteristics of the sensor are related to the initial resistance of semiconductor metal oxides. The influence of temperature and nanoscale heterojunction on oxygen adsorption will change the initial resistance of semiconductor metal oxides. The possible sensing mechanism model for SnO_2/Co_3O_4-based sensors is shown in Fig. 11.

When the p-Co_3O_4 is exposed to air, oxygen molecules adsorb on the surface of the Co_3O_4 and capture electrons from the electron hole pair of Co_3O_4, forming negative oxygen ion (O_2^-, O^-, O^{2-}); the overall reaction can be represented as

$$O_2\ (\text{gas}) \leftrightarrow O_2\ (\text{ads.}), \tag{2}$$

$$O_2\ (\text{ads.}) + e^- \leftrightarrow O_2^-\ (\text{ads.}), \tag{3}$$

$$O_2^-\ (\text{ads.}) + e^- \leftrightarrow 2O^-\ (\text{ads.}), \tag{4}$$

$$O^-\ (\text{ads.}) + e^- \leftrightarrow O^{2-}\ (\text{ads.}), \tag{5}$$

where ads. is the abbreviation for adsorbed. The hole concentration increases, and the hole accumulation layer (Fig. 11(a)) is formed on the surface of Co_3O_4. After contacting the reducing gas, the electron released from the desorption of negative oxygen ion forms a holeelectron pair. The electron released can be explained as[44]

$$CH_3CH_2OH + 2O^{2-}\ (\text{ads.}) \rightarrow CO_2\ (\text{gas}) + H_2O\ (\text{gas}) + 2e^{-}. \quad (6)$$

The hole concentration on the surface of the semiconductor decreases. That is why the resistance of Co_3O_4 increases when Co_3O_4 contacts the reducing gas. When n-SnO_2 is exposed to air, oxygen molecules adsorb on the surface of the SnO_2, oxygen molecules capture electrons from the surface of SnO_2 to form negative oxygen ion (O^{2-}, O^{-}, O_2^{-}), so electron depletion layer (Fig. 11(a)) is formed on the surface of SnO_2. After contacting the reducing gas, the negative oxygen ion desorbs, and the electron concentration on the surface of the semiconductor increases. That is why the resistance of SnO_2 decreases when SnO_2 contacting the reducing gas.

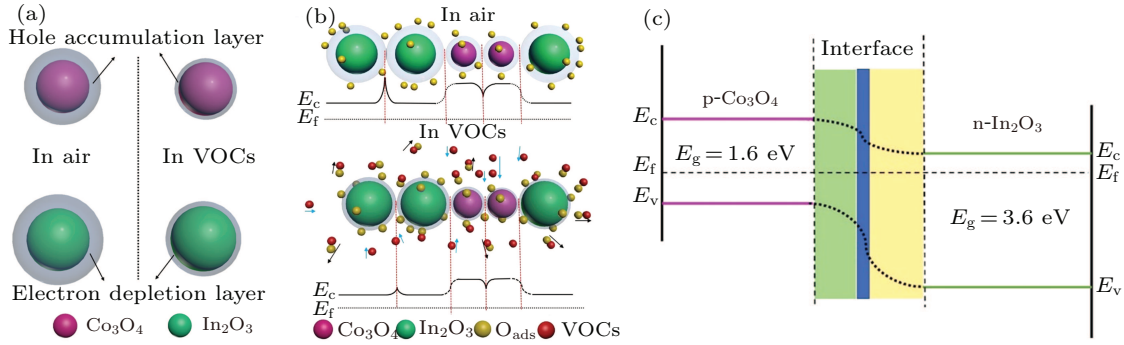


Fig. 11. (a) Sensing mechanism of SnO_2 and Co_3O_4 in air and in VOCs, (b) schematic diagram of nanoscale p-Co_3O_4/n-SnO_2 heterojunction, n-SnO_2/n-SnO_2 homojunction and p-Co_3O_4/p-Co_3O_4 homojunction in air and in VOCs, and (c) energy band diagram of SnO_2-Co_3O_4 system.

When the temperature is raised, the concentration of semiconductor carriers will increase, and more negative oxygen ions will be adsorbed on the sensor surface, so the response will be enhanced after having contacted the reducing gas. However, when the temperature is too high, the affinity energy of gas molecules is less than the work function of the metal–oxide–semiconductor surface. Then the electrons will transfer from the adsorbed negative ions to the semiconductor surface, and the adsorbed negative ions will reduce the hot spots on the semiconductor surface due to the loss of electrons, and thus the response is low after having contacted the reducing gas. Therefore, different semiconductor–metal–oxide sensors have different optimal operating temperatures.[45–47]

According to the HRTEM, nanoscale p-Co_3O_4/n-SnO_2 heterojunctions, n-SnO_2/n-SnO_2 homojunctions, and p-Co_3O_4/p-Co_3O_4 homojunctions exist in SnO_2/Co_3O_4 NFs. The schematic diagram is shown in Fig. 11(b). The nanoscale p–n heterojunction plays an important role in improving the gas sensing properties of composite materials.[26,48,49] The Fermi energy levels of n-SnO_2 and p-Co_3O_4 are different.[30,32,33,50] When the two kinds of NFs are combined, the electrons move from n-SnO_2 (work function 4.9 eV) to p-Co_3O_4 (work function 6.1 eV) due to the Fermi energy level equilibrium effect.[51] The electron depletion layer is formed on the SnO_2 side, and the hole is transferred from p-Co_3O_4 to n-SnO_2. The hole depletion layer is formed on the Co_3O_4 side. The space charge layer of n-SnO_2/p-Co_3O_4 is formed, and the energy bands on both sides are bent (Fig. 11(c)), resulting in the potential barrier, which greatly narrows the electron transport channel and reduces the conductivity,[52] as shown in Fig. 11(c). The existence of space charge layer can enhance the adsorption capacity of oxygen and make nanoscale p–n heterojunction become a hot spot after having contacted the reducing probe gas. When the SnO_2/Co_3O_4 sensors contact the reducing gas, the electrons released from the reactions of reducing gas and the desorption of negative oxygen ion will result in great resistance change, thereby reducing the potential barrier height.

4. Conclusions

The SnO_2/Co_3O_4 NFs with the hollow structure are prepared by homopolar doublejet electrospinning. The SnO_2/Co_3O_4 NFs gas sensor has good ethanolsensing properties at 250 °C. The formation mechanism of SnO_2/Co_3O_4 NFs' hollow structure is analyzed. The results show that the SnO_2/Co_3O_4 NFs have better reproducibility than the SnO_2. The optimum operating temperature of SnO_2/Co_3O_4 NFs is 250 °C, which is 100 °C lowers than that of SnO_2 NFs. The mechanism of gas sensing is analyzed. The SnO_2/Co_3O_4 NFs form nanoscale p–n heterojunction, which produces new hot spots to adsorb oxygen and improves its initial resistance. In addition, the method of homopolar doublejet electrospinning can be used for preparing other composite materials by changing the content of doping in the future work, which will be conducive to the quantitative research of the enhanced gas sensing performance of electrochemical gas sensors.

References

[1] Kou X, Wang C, Ding M, Feng C, Li X, Ma J, Zhang H, Sun Y and Lu G 2016 *Sens. Actuators B* **236** 425

[2] Burgués J and Marco S 2018 *Sensors* **18** 339

[3] Liu X, Chen N, Han B, Xiao X, Chen G, Djerdj I and Wang Y 2015 *Nanoscale* **7** 14872

[4] Suematsu K, Shin Y, Hua Z, Yoshida K and Shimanoe K 2014 *ACS Appl. Mater. Interfaces* **6** 5319

[5] Yan Z, He X L, Li J P, Jian J and Gao X G 2012 *Chin. Phys. Lett.* **29** 070701

[6] Panahi N, Shirazi M and Ghoranneviss M 2016 *Chin. Phys. Lett.* **33** 066802

[7] Hsueh T J, Peng C H and Chen W S 2019 *Sens. Actuators B* **304** 127319

[8] Li Y Z, Feng Q J, Shi B, Gao C, Wang D Y and Liang H W 2020 *Chin. Phys. B* **29** 018102

[9] Wei A, Wang Z, Pan L H, Li W W, Xiong L, Dong X C and Huang W 2011 *Chin. Phys. Lett.* **28** 080702

[10] Xu L, Wang R, Liu Y and Dong L 2011 *Chin. Phys. Lett.* **28** 040701

[11] Ma J, Fan H, Zhang W, Sui J and Wang S 2019 *Sens. Actuators B* **305** 127456

[12] Geng W, Ma Z, Zhao Y, Yang J, He X, Duan L, Li F, Hou H and Zhang Q 2020 *Sens. Actuators B* **325** 128775

[13] Fujihara S, Maeda T, Ohgi H, Hosono E and Kim S H 2004 *Langmuir* **20** 6476

[14] Hernández-Ramírez F, Tarancón A, Casals O, Arbiol J, Romano-Rodríguez A and Morante J R 2007 *Sens. Actuators B* **121** 3

[15] Yoon J W, Choi S H, Kim J S, *et al.* 2016 *NPG Asia Mater.* **8** e244

[16] Umar A, Ammar H Y, Kumar R, Ibrahim A A and Al-Assiri M S 2020 *Sens. Actuators B* **304** 127352

[17] Zhou Q, Xu L, Umar A, Chen W and Kumar R 2018 *Sens. Actuators B* **256** 656

[18] Mudra E, Shepa I, Milkovic O, Dankova Z and Dusza J 2019 *Appl. Surf. Sci.* **480** 876

[19] Liu T, Yu Z, Liu Y, Gao J and Liu F 2020 *Sens. Actuators B* **318** 128167

[20] Kou X, Meng F, Chen K, Wang T and Lu G 2020 *Sens. Actuators B* **320** 128292

[21] Guo J, Li Y, Jiang B, Gao H and Lu G 2020 *Sens. Actuators B* **310** 127780

[22] Park K R, Cho H B, Lee J, Song Y and Choa Y H 2019 *Sens. Actuators B* **302** 127179

[23] Wang D, Tang M, Fang H and Sun J 2020 *Sens. Actuators B* **318** 128290

[24] Bai S, Guo W, Sun J, Jiao L, Ye T, Chen A, Luo R and Li D 2016 *Sens. Actuators B* **226** 96

[25] Motaung D E, Mhlongo G H, Makgwane P R, Dhonge B P and Ray S S 2018 *Sens. Actuators B* **254** 984

[26] Park S H, Kim B Y, Jo Y K, Dai Z and Lee J H 2020 *Sens. Actuators B* **309** 127805

[27] Yu X X, Liu X S, Wu M Z, Sun Z Q, Li G and Chen X S 2014 *J. Phys. Chem. C* **27** 99

[28] Kou X, Wang C, Ding M, Feng C, Li X, Ma J, Zhang H, Sun Y and Lu G 2016 *Sens. Actuators B* **236** 425

[29] Choi S W, Jung S H and Kim S S 2011 *Nanotechnology* **22** 225501

[30] Kim J H, Lee J H, Mirzaei A, Kim H W and Kim S S 2017 *Sens. Actuators B* **248** 500

[31] Vladimirova S A, Rumyantseva M N, Filatova D G, Chizhov A S, Khmelevsky N O, Konstantinova E A, Kozlovsky V F, Marchevsky A V, Karakulina O M and Hadermann J 2017 *J. Alloys Compd.* **721** 249

[32] Tang W, Li D W, Du X J, Yu J and Sun Q Q 2019 *IOP Conference Series: Materials Science and Engineering* **479** 012116

[33] Bai S, Liu H, Luo R, Chen A and Li D 2014 *RSC Adv.* **4** 62862

[34] Du H, Yao P, Sun Y, Wang J and Wang H 2017 *Sensors* **17** 1822

[35] Liu C B, He Y and Wang S L 2015 *Chin. Phys. B* **24** 118501

[36] Ziabari M, Mottaghitalab V, Mcgovern S T and Haghi A K 2008 *Chin. Phys. Lett.* **25** 3071

[37] Du H, Wang J, Su M, Yao P and Yu N 2012 *Sens. Actuators B* **166–167** 746

[38] Kong J, Tan H R, Tan S Y, Li F, Wong S Y, Li X and Lu X 2010 *Chem. Commun. Roy. Soc. Chem.* **46** 8773

[39] Xia X, Dong X J, Wei Q F, Cai Y B and Lu K Y 2012 *Express Polym. Lett.* **6** 169

[40] Xiang H, Long Y, Yu X, Zhang X, Zhao N and Xu.J 2011 *CrystEngComm* **13** 4856

[41] Zafeiratos S, Dintzer T, Teschner D, Blume R, Knop-Gericke A and Schl G R 2010 *J. Catal.* **269** 309

[42] Xu Y, Ma T, Zheng L, Sun L and Zhang J 2018 *Sens. Actuators B* **284** 202

[43] Tang W, Yao M, Deng Y, Li X, Han N, Wu X and Chen Y 2016 *Chem. Eng. J.* **306** 709

[44] Liu J, Wang C, Yang Q, Gao Y, Zhou X, Liang X, Sun P and Lu G 2016 *Sens. Actuators B* **224** 128

[45] Yang F and Guo Z 2015 *J. Colloid Interface Sci.* **448** 265

[46] Kim H J and Lee J H 2014 *Sens. Actuators B* **192** 607

[47] Gardon M and Guilemany J M 2013 *J. Mater. Sci. Mater. Electron.* **24** 1410

[48] Wang Z, Li Z, Sun J, Zhang H, Wang W, Zheng W and Wang C 2010 *J. Phys. Chem. C* **114** 6100

[49] Mashock M, Yu K, Cui S, Mao S and Chen J 2012 *ACS Appl. Mater. Interfaces* **4** 4192

[50] Vladimirova S A, Rumyantseva M N, Filatova D G, Chizhov A S, Khmelevsky N O, Konstantinova E A, Kozlovsky V F, Marchevsky A V, Karakulina O M and Hadermann J 2017 *J. Alloys Compd.* **721** 249

[51] Rumyantseva M N, Vladimirova S A, Vorobyeva N A, Giebelhaus I and Gaskov A M 2018 *Sens. Actuators B* **255** 564

[52] Ju D, Xu H, Qiu Z, Zhang Z, Xu Q, Zhang J, Wang J and Cao B 2015 *ACS Appl. Mater. Interfaces* **7** 19163